

Article

Changes and Predictions of Vertical Distributions of Global Light-Absorbing Aerosols Based on CALIPSO Observation

Zigeng Song^{1,2}, Xianqiang He^{1,2,3,4,*}, Yan Bai^{1,2,3,4}, Difeng Wang², Zengzhou Hao², Fang Gong² and Qiankun Zhu²

¹ College of Oceanography, Hohai University, Nanjing 210098, China; 190811080001@hhu.edu.cn (Z.S.); baiyan@sio.org.cn (Y.B.)

² State Key Laboratory of Satellite Ocean Environment Dynamics, Second Institute of Oceanography, Ministry of Natural Resources, Hangzhou 310012, China; dfwang@sio.org.cn (D.W.); hzyx80@sio.org.cn (Z.H.); gongfang@sio.org.cn (F.G.); zhuqiankun@sio.org.cn (Q.Z.)

³ Southern Marine Science and Engineering Guangdong Laboratory (Guangzhou), Guangzhou 510000, China

⁴ School of Oceanography, Shanghai Jiao Tong University, Shanghai 200030, China

* Correspondence: hexianqiang@sio.org.cn

Received: 5 August 2020; Accepted: 14 September 2020; Published: 16 September 2020



Abstract: Knowledge of the vertical distribution of absorbing aerosols is crucial for radiative forcing assessment, and its quasi real-time prediction is one of the keys for the atmospheric correction of satellite remote sensing. In this study, we investigated the seasonal and interannual changes of the vertical distribution of global absorbing aerosols based on satellite measurement from the Cloud-Aerosol Lidar and Infrared Pathfinder Satellite Observations (CALIPSO) and proposed a neural network (NN) model to predict the vertical distribution of global absorbing aerosols. Gaussian fitting was proposed to derive the maximum fitted particle number concentration (MFNC), altitude corresponding to MFNC (MFA), and standard deviation (MFASD) for vertical distribution of dust and smoke aerosols. Results showed that higher MFA values of dust and smoke aerosols mainly occurred over deserts and tropical savannas, respectively. For dust aerosol, the MFA is mainly observed at 0.5 to 6 km above deserts, and low MFNC values occur in boreal spring and winter while high values in summer and autumn. The MFA of smoke is systematically lower than that of dust, ranging from 0.5 to 3.5 km over tropical rainforest and grassland. Moreover, we found that the MFA of global dust and smoke had decreased by 2.7 m yr^{-1} (statistical significance $p = 0.02$) and 1.7 m yr^{-1} ($p = 0.02$) over 2007–2016, respectively. The MFNC of global dust has increased by $0.63 \text{ cm}^{-3} \text{ yr}^{-1}$ ($p = 0.05$), whereas that of smoke has decreased by $0.12 \text{ cm}^{-3} \text{ yr}^{-1}$ ($p = 0.05$). In addition, the determination coefficient (R^2) of the established prediction models for vertical distributions of absorbing aerosols were larger than 0.76 with root mean square error (RMSE) less than 1.42 cm^{-3} , which should be helpful for the radiative forcing evaluation and atmospheric correction of satellite remote sensing.

Keywords: absorbing aerosol; vertical distribution; long-term change; prediction model; CALIPSO

1. Introduction

Light-absorbing aerosols play a vital role in Earth's radiative forcing, global climate change, and atmospheric correction of satellite remote sensing [1–3]. In addition to scattering effect, they absorb solar radiation, thereby decreasing the reflected radiance at the top of the atmosphere (TOA), cooling the Earth's surface, and heating the atmosphere [4,5]. For example, the standard atmospheric correction algorithm for satellite ocean color remote sensing assumes that all of the aerosols reside in the bottom

of the two-layer atmosphere, and aerosol radiance contributions are generally overestimated which would lead to the underestimation of the retrieved normalized water-leaving radiance under the influence of absorbing aerosols, especially at the short visible light bands [6–8]. From an environmental perspective, absorbing aerosols have a profound impact on the hydrological and carbon cycles, as well as environmental issues such as acid rain and tropospheric ozone pollution [9]. Therefore, it is essential to explore and gain comprehensive knowledge about absorbing aerosols on a global scale.

Absorbing aerosols principally consist of dust, black carbon, and organic carbon aerosols. With increasing anthropogenic emissions worldwide, absorbing aerosols have changed not only in concentration but also in vertical distribution [10]. Moreover, the rise in air temperature and uneven distribution of convective precipitation appears to be driven by absorbing aerosols in some regions [11]. In recent decades, sophisticated methods to observe absorbing aerosol profiles have been developed using ground- and satellite-based measurements [12]. Ground-based platforms can only observe regional variations, and the satellite measurements are an important way for global scale observations. For example, based on satellite observations by the Ozone Monitoring Instrument (OMI), Kang et al. (2017) investigated the spatial and temporal distribution of absorbing aerosols and found an increase in absorbing aerosols over the East Asia [13]. Han et al. (2015) found a high correlation between aerosol optical depth (AOD) and particulate matter (PM) based on satellite observations from the Moderate Resolution Imaging Spectroradiometer (MODIS) [14]. Guo et al. (2011) analyzed spatiotemporal variation trends in AOD in China based on Total Ozone Mapping Spectrometer (TOMS) and MODIS data and found a significant increase in AOD during the period 1980–2008 [15]. However, OMI and MODIS aerosol products can only provide columnar aerosol optical properties [16].

The Cloud-Aerosol Lidar with Orthogonal Polarization (CALIOP) onboard the Cloud-Aerosol Lidar and Infrared Pathfinder Satellite Observations (CALIPSO) satellite, which was launched on 28 April 2006 [17], allows for observation of vertical profile information for different types of aerosols at global scale. For example, Cavalieri et al. (2011) investigated seasonal and interannual variation in aerosol optical properties and vertical distribution of aerosols in the Sahel from 2006 to 2008 [18]. Huang et al. (2015) examined the most probable height of aerosols and their seasonal variations in six high-aerosol-loading regions [19]. In addition, CALIOP data revealed that smoke aerosols were primarily composed of organic carbon aerosols (50–70%) and black carbon aerosols (5–15%) [20]. Although CALIOP has the capability to provide some information about the composition of absorbing aerosols, it still unable to provide quasi real-time and high spatiotemporal resolution aerosol product for the atmospheric correction of satellite remote sensing data due to long revisiting period (~16 days) and only along track observation [8]. Recently, Yao et al. (2019) developed a random forests model to predict the minimum height of smoke layer based on CALIPSO measurements, but they only provided the predictions along the coast of Canada instead of the global scale [21]. Thus, it is necessary to explore quasi real-time predictions on the vertical distributions of global absorbing aerosols, which is the key for the atmospheric correction of satellite remote sensing.

However, the vertical distributions of absorbing aerosols are nonlinearly influenced by aerosol emissions, multiple meteorological, and radiative factors, which leads to the difficulty of predictions. As for the complex nonlinear problems, neural network (NN) models can outperform most of traditional numerical models and empirical statistical methods [22]. Previous atmospheric aerosol studies have forecast the aerosol optical depth (AOD) [23] and some environmental parameters such as dust storm and PM_{2.5} (respirable particulate matter with aerodynamic diameter below 2.5 mm) concentrations based on NN models [24–26]. Their results show that the NN models can well leverage the spatiotemporal correlations and reach a minimum error by training model, therefore, which can be adopted in the prediction on the vertical structures of absorbing aerosols.

Overall, compared to spatiotemporal distributions, the vertical distributions of absorbing aerosols have been less investigated at global scale [27–29]. Moreover, under a global change background, the long-term changes in absorbing aerosol vertical distribution remain poorly known. In this study, based on time-series observed by CALIPSO, we investigated the seasonal and interannual variations

in the vertical distribution of absorbing aerosols at the global scale from 2006 to 2016, and established prediction model for the vertical distributions of absorbing aerosols. Section 2 provides the data and methods for deriving vertical distribution parameters for the absorbing aerosols, and the establishment of the prediction model. Section 3 presents results on the seasonal variations, long-term changes, and predictions in vertical distributions of absorbing aerosols. Sections 4 and 5 provide discussion and conclusions, respectively.

2. Data and Methods

2.1. Data Preparation

The principal limitation for investigating global vertical distributions of absorbing aerosols is the lack of simultaneously and continuously available data. CALIPSO is able to conquer this limitation due to its capability to observe aerosol profiles ceaselessly during the day and night. CALIOP, which is the principal sensor onboard the CALIPSO satellite of the NASA A-Train constellation since May 2006, is the first dual-wavelength orthogonal polarization lidar to observe the profiles of aerosols and clouds on a global scale. The CALIPSO satellite has a revisiting period of 16 days and provides near-global coverage between 82°S and 82°N for the study of clouds and aerosols. CALIOP V3 discriminates aerosols into six types (clean marine, dust, polluted continental, clean continental, polluted dust, and smoke) based on layer-integrated attenuated backscatter, volume depolarization ratio, and type of underlying surface [30].

In this study, we obtained the time-series CALIPSO global monthly aerosol product from June 2006 to December 2016 from <http://eosweb.larc.nasa.gov/>. “Aerosol_Type” provides aerosol particle number concentration at high vertical resolution (60 m) from −0.5 to 12 km above sea level with a horizontal resolution of 5° (longitude) × 2° (latitude) [31]. Overall, the monthly aerosol product is a four-dimensional array (85 × 72 × 208 × 6), corresponding to latitude, longitude, altitude, and aerosol type, respectively. In this study, we focused on two absorbing aerosol types, i.e., dust (polluted dust included) and smoke.

We also obtained the atmospheric environment dataset from the European Centre for Medium-Range Weather Forecast (ECMWF) atmospheric reanalysis of the global climate (ERA5) to predict the vertical distributions of absorbing aerosols, which was available at the Copernicus Climate Change Service (C3S) website (<https://cds.climate.copernicus.eu#!/home>). ERA5 products contain hourly and monthly data with 0.25° grid resolutions from January 1979 to present. In addition, mean altitude of biomass burning emissions injection and dust aerosol layer height were used to validate daily model prediction results, which were acquired from the Global Fire Assimilation System (GFAS) of the Copernicus Atmosphere Monitoring Service (CAMS) and the Infrared Atmospheric Sounding Interferometer (IASI) onboard Meteorological Operational Satellite Program A (MetOp-A) products, respectively [32,33]. These products can be obtained from ECMWF website (<https://apps.ecmwf.int/datasets/>) and C3S website.

2.2. Retrieval of Vertical Distribution Parameters

As the aerosol particle number concentration is roughly a Gaussian distribution in the vertical direction [34], here we used the Gauss curve fitting to retrieve the parameters of vertical distribution for both dust and smoke aerosols, as shown in the green box of Figure 1. Firstly, at each grid, the particle number concentrations of the vertical profile for both dust and smoke aerosols were normalized by the maximum values before the Gauss curve fitting. Then, the normalized particle number concentration was fitted by the Gauss function for each aerosol type as:

$$N_i = N_{m,i} \exp \left[\frac{-(h_i - h_{m,i})^2}{2\sigma_i^2} \right], \quad (1)$$

where i is the index in altitude direction; $N_{m,i}$ is the fitted maximum normalized particle number concentration; $h_{m,i}$ is the altitude corresponding to the maximum number concentration; and σ_i is the standard deviation. Finally, the maximum fitted particle number concentration $N_{m,i}^*$ can be estimated by:

$$N_{m,i}^* = \max(N_{aerosol_type,i}^*) \cdot N_{m,i}, \tag{2}$$

where $N_{aerosol_type,i}^*$ is the profile of particle number concentration observed by CALIPSO. For each grid in the monthly product, $N_{m,i}^*$, $h_{m,i}$, and σ_i were retrieved for dust and smoke aerosols, respectively. To eliminate the influence of noise on the final statistical results, we performed quality control using the determination coefficient (R^2) of Gaussian fitting. Specifically, $N_{m,i}^*$, $h_{m,i}$, and σ_i with $R^2 \geq 0.5$ were adopted for further statistical analyses, which retained 84.3% of the dust dataset and 78.1% of the smoke dataset.

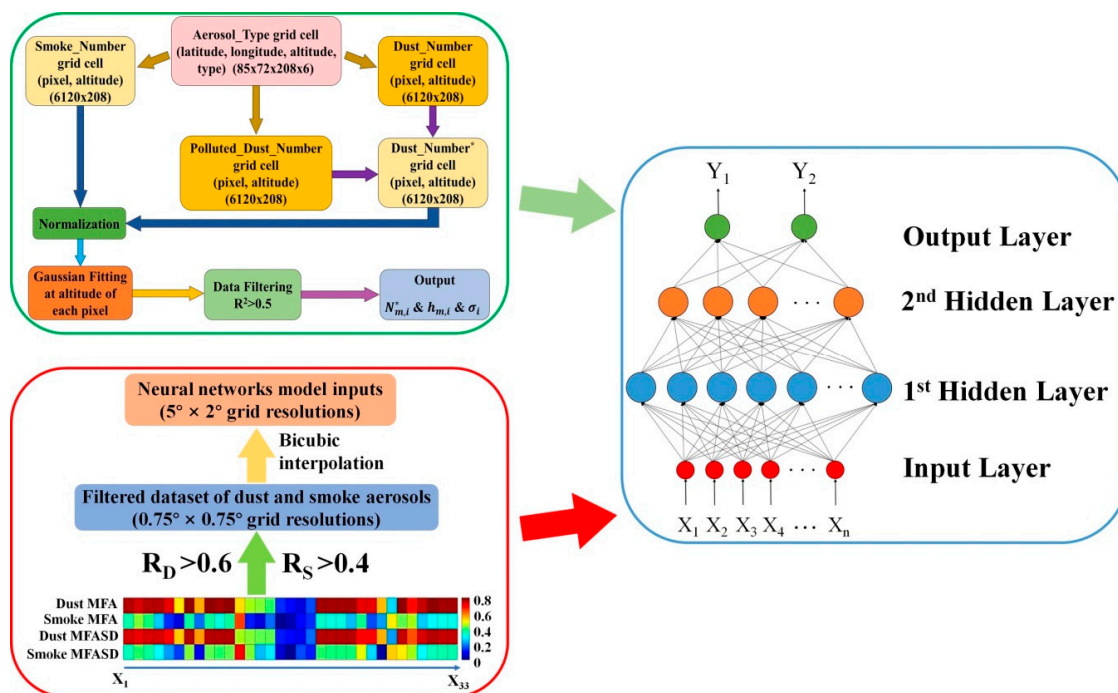


Figure 1. Flow chart of the retrieval process of absorbing aerosol vertical distribution parameters based on Gauss curve fitting and NN models. Green box presents the Gauss curve fitting process. Red box presents the data preprocess. Blue box presents the NN model.

To quantitatively investigate the spatiotemporal distribution of absorbing aerosols in different seasons, years, and regions, we determined the temporal and regional mean $N_{m,i}^*$ (maximum fitted particle number concentration, named as MFNC), mean $h_{m,i}$ (altitude corresponding to MFNC, named as MFA), and mean σ_i (standard deviation, named as MFASD) for further analysis. Before considering the long-term changing trends of absorbing aerosols, however, a significant handicap should be noted. Specifically, since MFNC is the absolute particle number concentration, we are unable to compare the rate of changes for different magnitudes of MFNC as high MFNC values usually have a larger absolute rate than low MFNC values. Consequently, we use the relative change rate in MFNC instead of the absolute change rate. The absolute change rates of MFA and MFNC were first calculated by linear regressions, with the t -test then applied to verify statistical significance. The mean values of MFA and MFNC were then used to obtain the relative change rates. For example, the rate of relative change in MFNC was calculated as:

$$v_r = \frac{v_a}{MFNC}, \tag{3}$$

where v_a is absolute rate of change in MFNC, which is equal to the slope calculated by linear regression, and \overline{MFNC} is the mean value of MFNC.

2.3. Development of the Prediction Model

In this study, two different NN models were established to predict global vertical distribution parameters (MFA and MFASD) of dust and smoke aerosols, respectively. The structure of the NN model contains three components (input layer, two hidden layers, and output layer), as shown in the blue box of Figure 1. Previous studies mainly used some meteorological factors correlated with the evolution of atmospheric aerosol such as relative humidity, wind speed, surface pressure, and temperature [22,23,35,36]. Since the model targets are relative with the vertical variations of meteorological factors [21], it is necessary to add vertically changing factors (e.g., boundary layer height, vertical integral of temperature, and relative humidity at different altitudes) into the input dataset. As Lakshmi et al. [37] found that the interannual variability in dust's AOD might be associated with the seasonal rainfall, it is important to consider the precipitation in model. In addition, column cloud liquid water and radiative parameters need to be added to input dataset due to the fact that aerosols have an influence in the nucleation of cloud water droplets and the radiance at the top of the atmosphere (TOA) [38,39].

Inputs to the NN model include reanalysis parameters, meteorological factors, and radiative parameters from the ERA5 products (Table 1). It should be noted that each pixel is treated independently in the model. Considering the volumes and varieties of meteorological factors are large, it is necessary to remove the parameters with little contribution to absorbing aerosol vertical distribution prediction. The number of neurons in the input layer is 22 and 23 for dust and smoke aerosols, respectively. Additionally, the quality of the NN model training dataset needs to be controlled by selecting 70 and 40 cm^{-3} as the minimum threshold of the dust's and smoke's particle number concentration. This data quality control can remove the records with quite low particle number concentrations, as these records may contain relative higher uncertainty due to detection ability limitation for low particle number by the CALIOP. Moreover, to improve the quality of the predicted results, we normalized the input and output dataset to avoid their significant differences.

During the training process, vertical distribution parameters of dust and smoke and atmospheric environment factors in odd number years from 2007 to 2016 were used to train and test the model, with 70%, 15%, and 15% of the total training dataset were divided into training subset, validation subset, and testing subset. In order to obtain a good performance, configuring the initial optimum parameters plays an important role in training the models. Therefore, we applied Levenberg-Marquardt (LM) backpropagation algorithm to train the network, and adapted gradient descent with momentum weight and bias (LEARNGDM), mean square error (MSE), hyperbolic tangent sigmoid (TANSIG), and linear (PURELIN) as adaption learning function, performance function, transfer functions of the hidden layer, and transfer functions of the output layer, respectively. The two hidden layers have 20 and 12 neurons based on the Guang-Bin Huang method [40]. The initial learning rate is first set 0.001, which can be updated over training iterations based on back-propagated stochastic gradient optimization. After the prediction model training was complete, we used independent dataset from another five years (even number years from 2007 to 2016) to validate the model. Moreover, the altitude of biomass burning emissions injection and dust aerosol derived from CAMS and IASI were adopted to validate model-predicted smoke and dust MFA on 1st January 2019, 1st April 2019, 1st June 2019, and 1st October 2019 to represent different seasons.

Table 1. Neural networks model inputs.

Input	Description	Input	Description
X1	Relative humidity at 1000 hPa	X18	Vertical integral of divergence of geopotential flux
X2	Relative humidity at 950 hPa	X19	Vertical integral of divergence of kinetic energy flux
X3	Relative humidity at 900 hPa	X20	Vertical integral of potential and internal energy
X4	Relative humidity at 850 hPa	X21	Vertical integral of temperature
X5	Relative humidity at 800 hPa	X22	Vertical integral of thermal energy
X6	Evaporation	X23	Vertical integral of water vapor
X7	Mean sea level pressure	X24	Albedo
X8	10 m wind speed	X25	Boundary layer height
X9	Skin temperature	X26	Surface roughness for heat
X10	Surface pressure	X27	Surface roughness
X11	Soil temperature	X28	Surface latent heat flux
X12	Volumetric soil water	X29	Surface sensible heat flux
X13	Total column cloud ice water	X30	Surface net solar radiation
X14	Total column cloud liquid water	X31	Surface solar radiation downwards
X15	Total precipitation	X32	Top net solar radiation
X16	10 m wind speed of U component	X33	Top net thermal radiation
X17	10 m wind speed of V component		

3. Results

3.1. Seasonal Variations in Dust Aerosols

Figure 2 presents the seasonal distributions of dust aerosol MFNC, calculated from monthly products obtained from CALIOP averaged over 2006–2016. Clearly, significant spatial variations were found, with larger MFNC values over land than over ocean, and dust aerosols mainly occurred in the North Africa, Middle East, and surrounding waters (Figure 2). Slightly higher MFNC values were also observed in East Asia, Indian subcontinent, and Mid-Atlantic. The dense dust aerosol load in the Sahara Africa and Arab areas was primarily attributed to the aerosol particles originating from the desert. Unlike some desert areas, the commensurate MFNC of dust aerosol appeared in China and India might not only be contributed by the dust sources from Gobi, but also be influenced by urban and industrial dust. Obvious seasonal variations were observed in Northeast China, Arabian Sea, Indian Peninsula, and their surroundings. Taking the North Sahara and North China as examples, we found higher MFNC values in boreal summer (from 280 to 360 cm^{-3}) than in winter (from 120 to 240 cm^{-3}) in the North Sahara, but the opposite in North China, with higher MFNC values in spring, autumn, and winter (from 120 to 260 cm^{-3}) than in summer (from 60 and 130 cm^{-3}). It should be noted that the Tibetan Plateau has no data in Figure 2 and following figures due to the failure of Gaussian fitting caused by the extremely high altitude.

The seasonal variations in MFA revealed significant regional characteristics, with the largest values in the Middle East and North Africa (MENA) in boreal autumn (Figure 3). Overall, relatively higher MFA values (upper to 2.2 km) were observed in boreal summer and autumn, likely due to the increase in atmospheric temperature [41]. Additionally, the highest MFA values were generally found on plateaus or mountains near deserts, such as East African Plateau, Qinghai Tibet Plateau, and Rocky Mountains. Concerning the global ocean, the MFA values were higher in the Antarctic Ocean and North Pacific than in other oceans, apart from seas near deserts. The maximum MFA in the different oceanic regions varied with different seasons; for example, the maximum in the North Pacific occurred during boreal summer (2.1 to 3.2 km) but occurred during autumn in the MENA region (3.3 to 4.1 km). These seasonal variation characteristics of MFA were also observed in other regions.

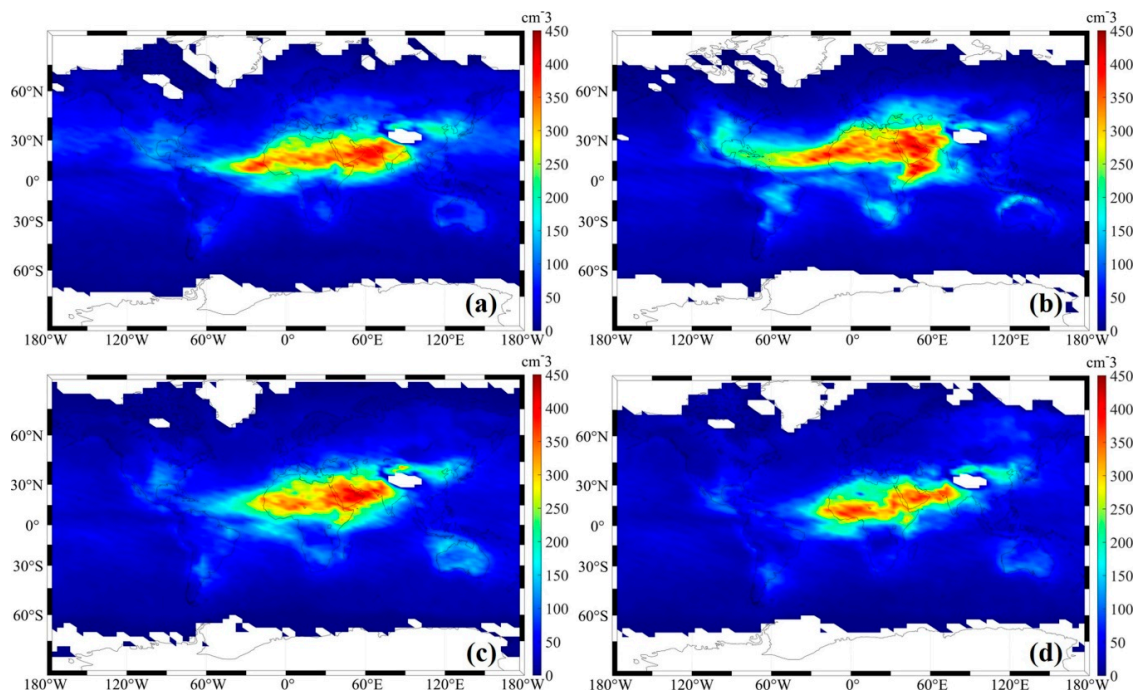


Figure 2. Spatial distributions of seasonal dust aerosol MFNC averaged from 2006 to 2016. (a) Spring; (b) summer; (c) autumn; (d) winter. White area indicates no data. It should be noted that the scale of color bars are different from each other.

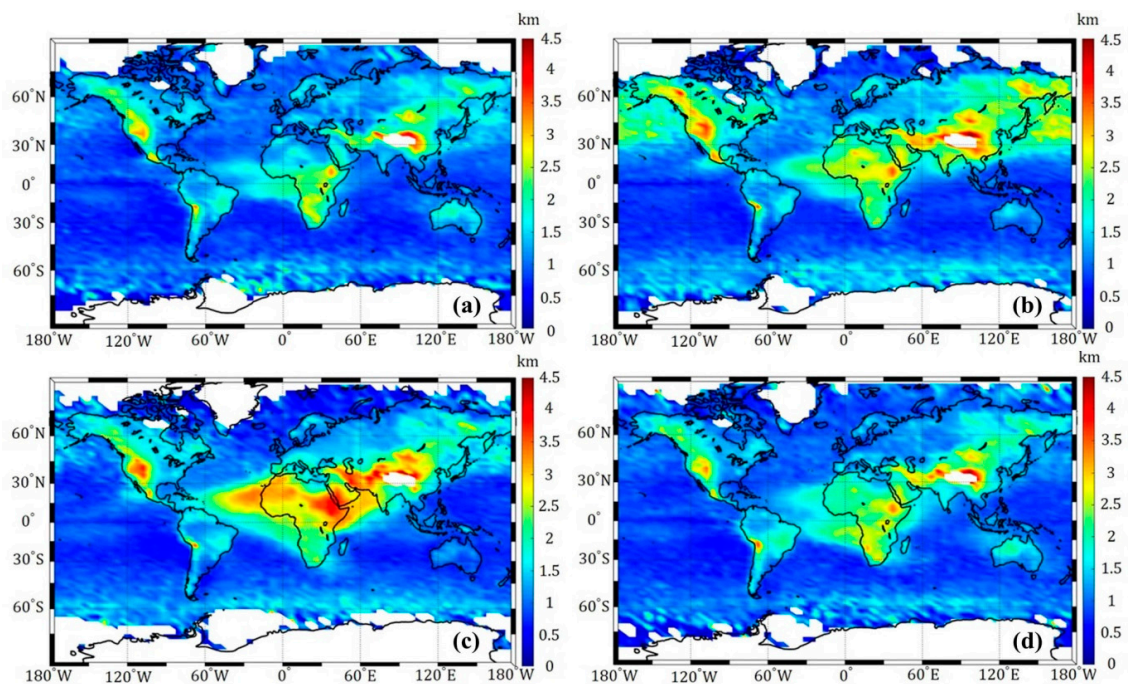


Figure 3. Same as Figure 2 but for the dust aerosol MFA.

Comparing Figures 2 and 3, seasonal variations in MFASD (Figure 4) were more obvious than those of MFA and MFNC. The MFASD values exhibited distinct seasonality, with relatively higher values in boreal spring and summer and generally lower values in autumn and winter. The lowest MFASD was observed in winter for most places worldwide. The high MFASD regions started to expand further to the west from boreal winter to summer; moreover, this pattern was enhanced by the

long-range transport of dust from the Western Sahara Desert over the Atlantic Ocean, which influenced the vertical profile of dust to a certain extent. We also estimated that dust was mainly distributed at 0.5 to 6 km over the Sahara Desert, Arabian Desert, and other deserts based on MFA (2 to 4.5 km) and MFASD (0.8 to 1.5 km).

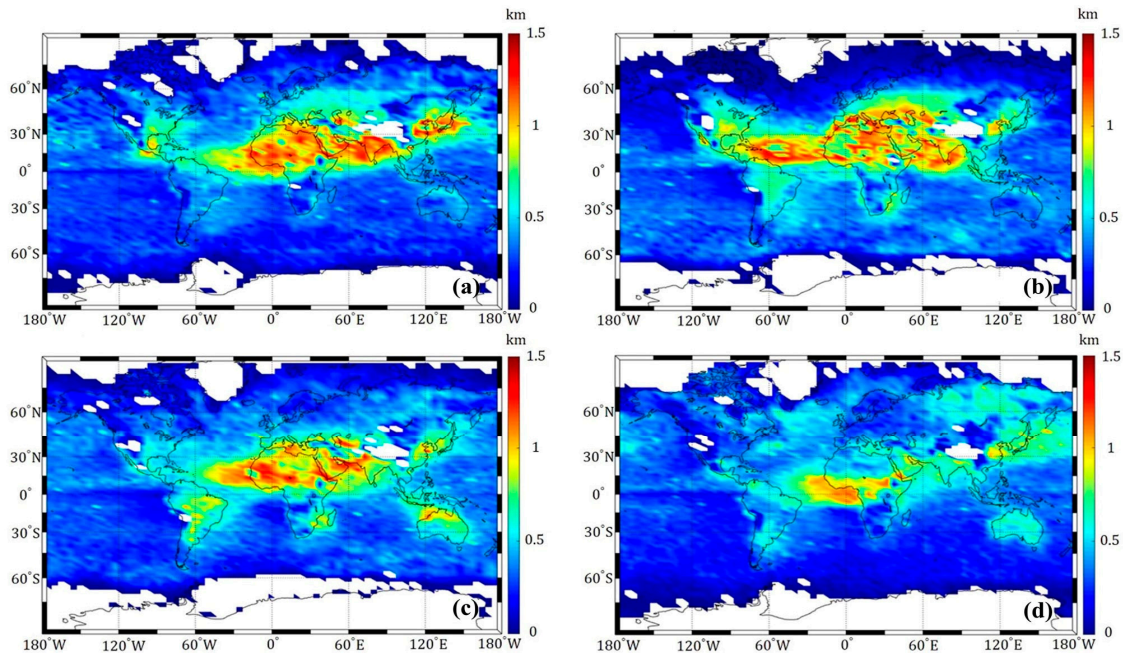


Figure 4. Same as Figure 2 but for the dust aerosol MFASD.

3.2. Seasonal Variations in Smoke Aerosols

Based on the spatial distributions of MFNC (Figure 5), we found that smoke aerosols mainly distributed in five regions: South-Central Africa, Southeast Asia, Amazon basin, Indian Peninsula, and Central American Isthmus. The largest seasonal variation in MFNC was found in South-Central Africa (150 to 400 cm^{-3} in boreal summer, 30 to 90 cm^{-3} in winter). Moreover, during boreal winter and spring, smoke aerosol particles were mainly observed in South and Southeast Asia, with MFNC values approaching that of South-Central Africa. The smoke aerosols were likely transported more strongly over the tropical Central American Isthmus during boreal spring and winter, resulting in high MFNC values (from 100 to 150 cm^{-3}).

Considering the seasonal variation in MFA (Figure 6), the highest values (ranging from 2.1 to 2.6 km) occurred in the Congo Basin during boreal autumn (Figure 6). Furthermore, in South-Central Africa, the coverage of high MFA values slightly transferred to the south from boreal autumn to winter. Comparing Figure 6 with Figure 3, fewer smoke particles were observed over the ocean due to their differences in microphysical properties and aging behaviors. In particular, the variation in smoke MFA over land contributed to that over nearby oceans and the range of influence partly depended on their effective distance from the source. Comparison of the four seasonal distributions (Figure 6) identified distinct seasonal variation characteristics, whereby high-latitude Northern Hemisphere regions with high smoke MFA moved to the south from boreal spring to summer and to the north from autumn to winter. This seasonal migration might be relevant to variance in temperature. High smoke MFA (~2.3 km) was also found in the Sino American Isthmus during boreal summer, which was quite different from that found in other regions.

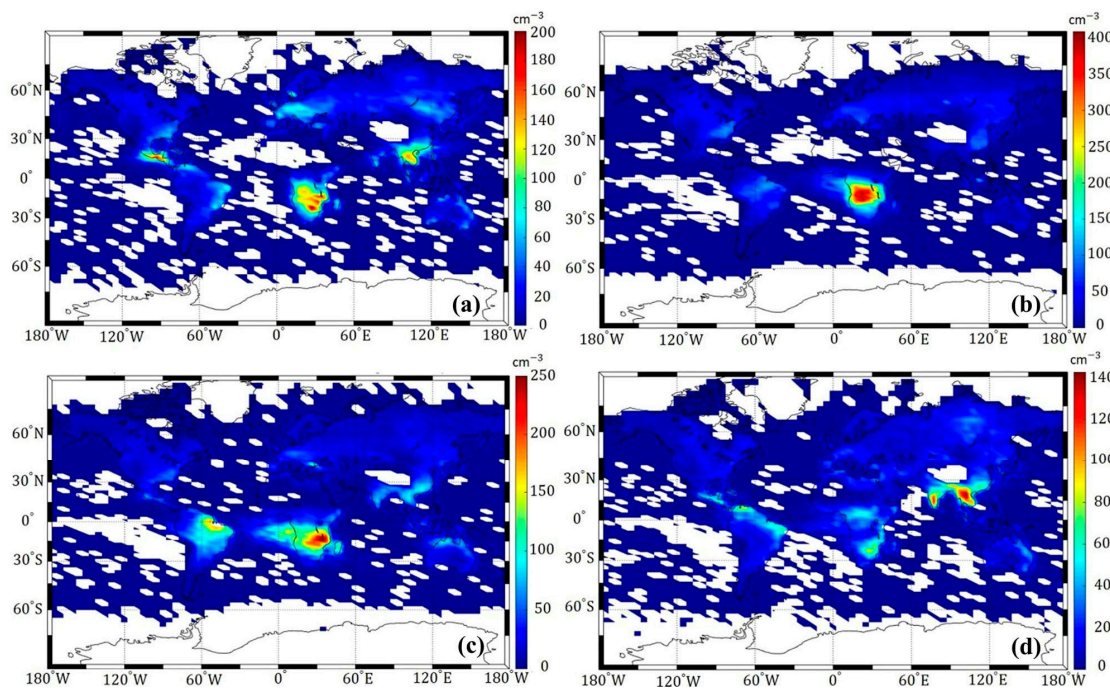


Figure 5. Spatial distributions of seasonal smoke aerosol MFNC averaged from 2006 to 2016. (a) Spring; (b) summer; (c) autumn; (d) winter. White area indicates no data. It should be noted that the scale of color bars is different from each other.

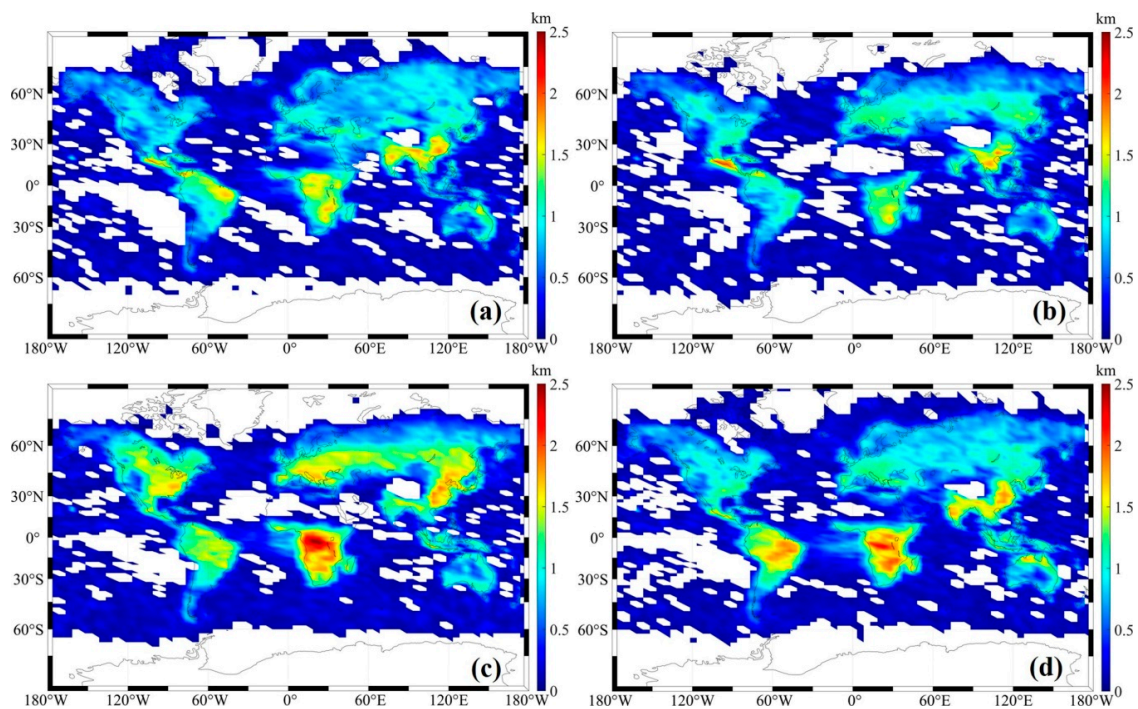


Figure 6. Same as Figure 5 but for the smoke aerosol MFA.

Overall, smoke MFASD was similar to MFA in spatial distribution (Figure 7). Intriguingly, we can integrate vertical characteristics and concentrations into the spatiotemporal distribution of smoke aerosols. Taking smoke in Southeast China as an example, 68.2% of smoke aerosols distributed at 0.6 to 2.6 km (i.e., smoke MFASD and MFA values were 0.6 to 0.8 km and 1.4 to 1.8 km, respectively, during boreal summer and autumn). In the same way, 68.2% of smoke aerosols were observed at 0.5 to

3.5 km above tropical savannas. Although comparatively large MFASD values were distributed at high latitudes, such as Eastern Siberia and western coasts of the Americas, the influence of smoke was expected to be small due to lower MFNC values in these regions.

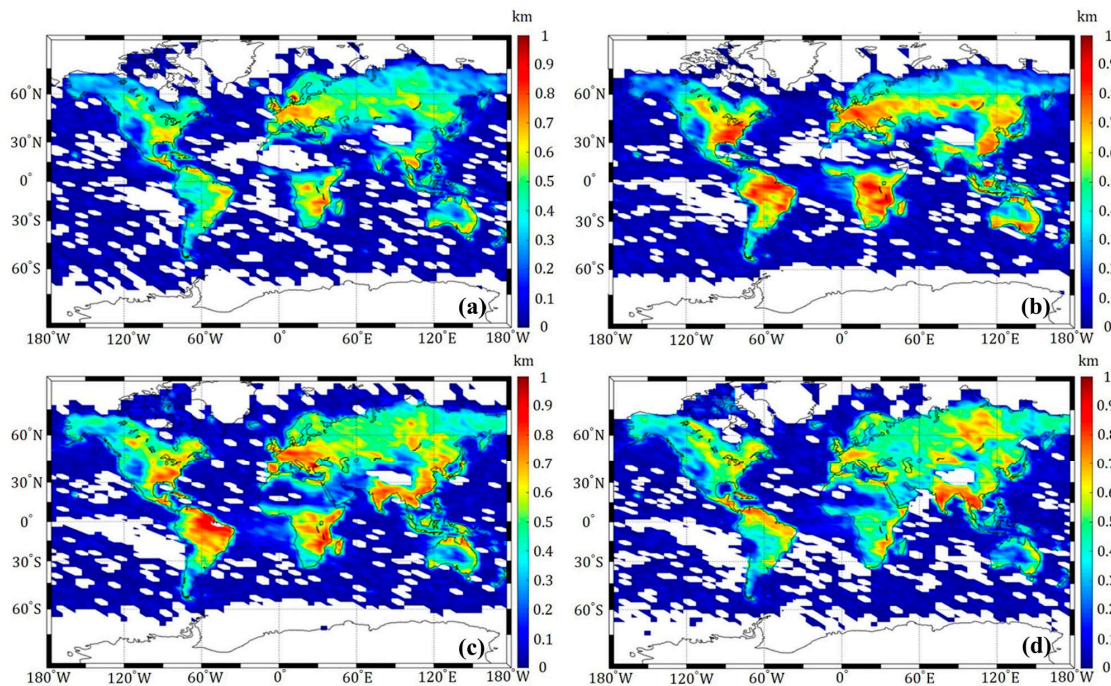


Figure 7. Same as Figure 5 but for the smoke aerosol MFASD.

3.3. Long-term Changes in Global Dust and Smoke Aerosols

Figure 8a–d show the linear trends of the monthly globally averaged MFA and MFNC values over 2007–2016, respectively. Overall, the MFA values of global dust and smoke aerosols both decreased significantly by 2.7 m yr^{-1} ($p = 0.02$, $R = 0.72$) and 1.7 m yr^{-1} ($p = 0.02$, $R = 0.70$), respectively. For particle number concentration, the global dust MFNC increased by $0.63 \text{ cm}^{-3} \text{ yr}^{-1}$ ($p = 0.05$, $R = 0.61$), whereas the global smoke MFNC decreased by $0.12 \text{ cm}^{-3} \text{ yr}^{-1}$ ($p = 0.05$, $R = 0.62$). Figure 9 presented the spatial distributions of changing rates in MFNC and MFA over 2007–2016. Overall, significantly decreasing trends in dust MFNC (-15 to -5 \% yr^{-1}) were observed in the North Pacific.

We further explored the differences in changing trends in MFA and MFNC over land and ocean. Overall, long-term changing trends of global MFA over land and ocean were consistent with the decreasing trend for absorbing aerosols, except for dust aerosols over land, as seen in Figure 8a. Specifically, dust MFA over land insignificantly increased by 0.2 m yr^{-1} ($p = 0.19$), but smoke MFA decreased significantly by 4.3 m yr^{-1} ($p = 0.05$). As absorbing aerosols mainly originate from land, the rate of change in MFNC over land was slightly higher than that of global mean, namely $0.98 \text{ cm}^{-3} \text{ yr}^{-1}$ ($p = 0.04$) and $-0.11 \text{ cm}^{-3} \text{ yr}^{-1}$ ($p = 0.23$) for dust and smoke, respectively. However, due to the systematic differences in MFA values between the ocean and land ($1.74 \pm 0.35 \text{ km}$ and $1.34 \pm 0.25 \text{ km}$ over land; $1.14 \pm 0.17 \text{ km}$ and $0.15 \pm 0.07 \text{ km}$ over ocean for dust and smoke, respectively), we also found differences in the rate of change in MFA. Over the ocean, dust and smoke MFA decreased significantly, i.e., 4.9 m yr^{-1} ($p = 0.004$) and 0.9 m yr^{-1} ($p = 0.04$), respectively. In contrast, MFNC increased over 2007–2016 for both land and ocean. Both dust and smoke MFNC increased significantly ($0.56 \text{ cm}^{-3} \text{ yr}^{-1}$, $p = 0.08$; $0.12 \text{ cm}^{-3} \text{ yr}^{-1}$, $p = 0.02$, respectively). Overall, the variations of absorbing aerosols were more significant over land than over ocean, regardless of MFA or MFNC. It should be noted that these changing trends might be affected by the uncertainty of the CALIPSO products as well as the relatively short observation period (2007–2016).

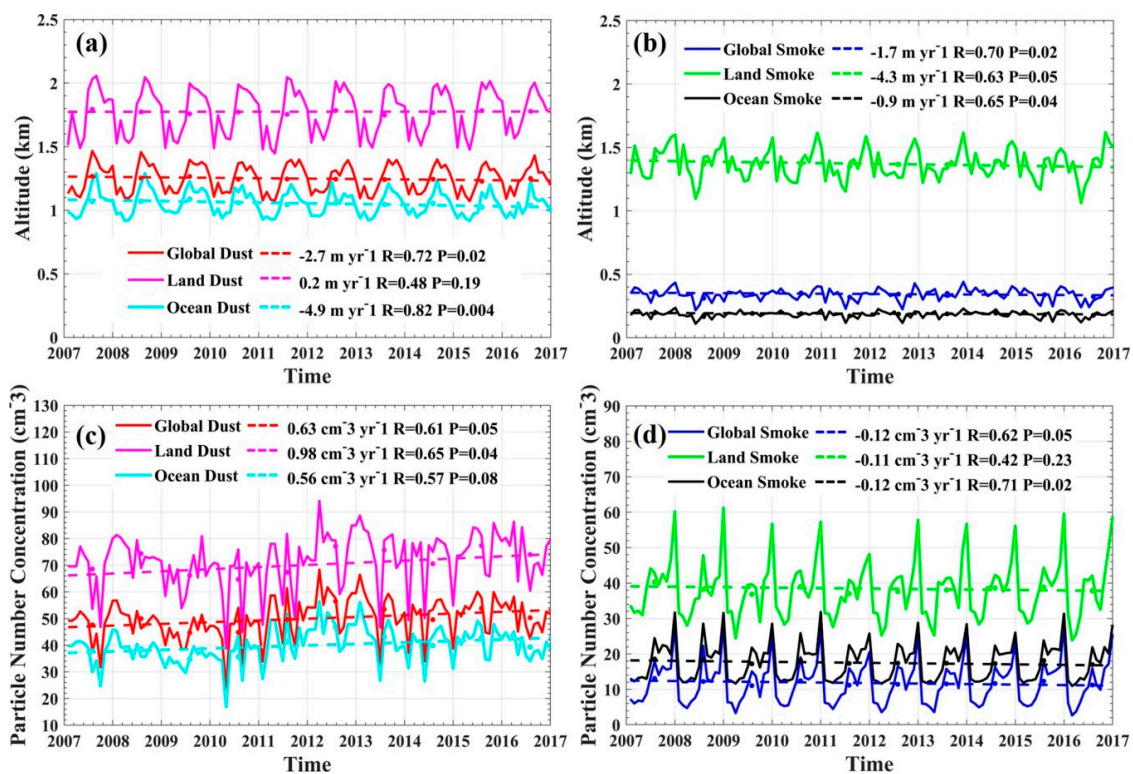


Figure 8. Variations in monthly (solid lines) and annual (circle points) mean MFA and MFNC values of absorbing aerosols from 2007 to 2016 for global, land and ocean. (a) MFA variations for dust; (b) Same as (a), but for smoke; (c) MFNC variations for dust; (d) same as (c), but for smoke.

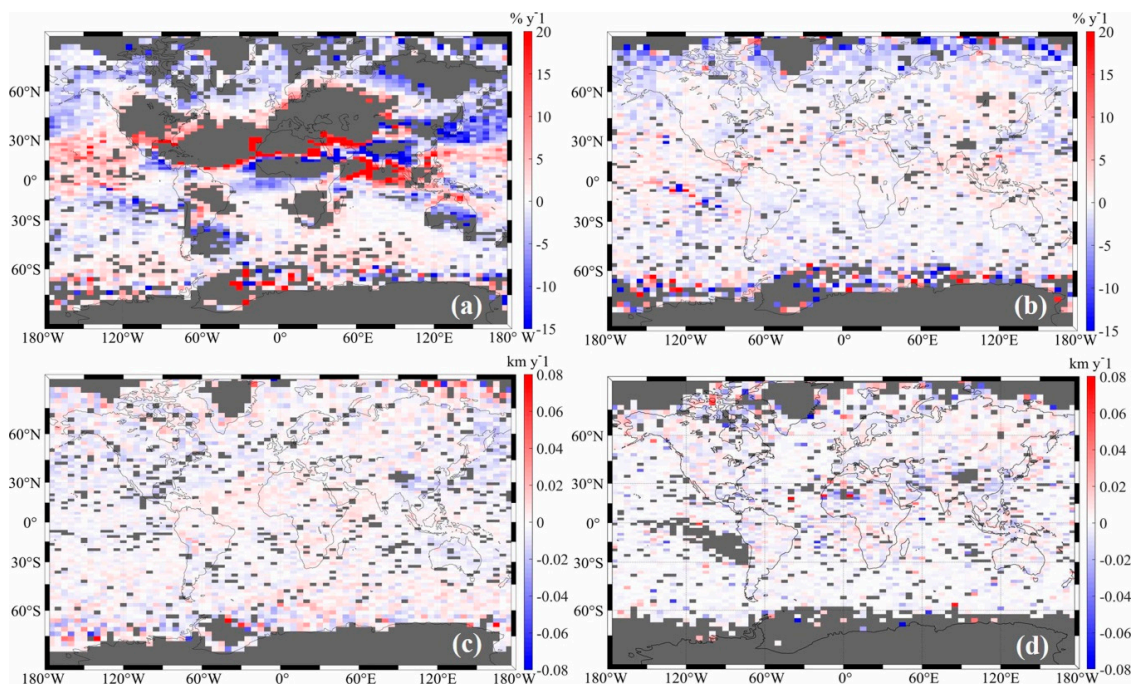


Figure 9. Spatial distribution in long-term rates of changes in absorbing aerosol MFA and MFNC values from 2007 to 2016. (a) The rates of change in MFNC for dust; (b) The rates of change in MFNC for smoke; (c) The rates of change in MFA for dust; (d) The rates of change in MFA for smoke. Gray shading indicates no data or failure of the significant test ($\geq 95\%$ confidence level). Note, scales of color bars are different from each other.

3.4. Prediction of Vertical Distributions of Absorbing Aerosols

Figure 10 showed the comparison between predicted dust MFA and MFASD and known values (CALIPSO observations) from the validation dataset. Overall, the predicted results were consistent with those observed by CALIPSO in both spatial pattern and magnitude. Moreover, the seasonal variations that higher MFA and MFASD values during boreal autumn and lower values during spring as revealed by the predicted results (Figure 10b,d) were similar to the CALIPSO measurements. Similarly, the prediction results of the smoke aerosol were generally coincident with the CALIPSO observations (validation dataset) (Figure 11), despite of slight underestimation for the predicted results especially in the regions with high MFA (up to 1.6 km) and MFASD (up to 0.6 km) in autumn.

Figure 12 provided the correlation coefficients between predicted values and validation dataset (CALIPSO observations) for dust aerosol, with 0.87 to 0.93 and 0.83 to 0.91 for MFA and MFASD, respectively. It needs to be noted that compared to the CALIPSO observations, the predicted results were relatively smoother, especially in the Central Atlantic Ocean, Northern Sahara Desert, Arabian Peninsula, and Arabian Sea, and the difference in boreal autumn was relatively larger than it in other seasons. As shown in Figure 13, the correlation coefficients between model predicted and CALIPSO observed values for the smoke aerosol were slightly lower than that of the dust aerosol, but still larger than 0.80 and 0.78 for the MFA and MFASD, respectively.

As shown in the Figure 14, the vertical profile of absorbing aerosols particle number concentration can be well reproduced from the MFA and MFASD predicted by the NN models, with determination coefficient (R^2) larger than 0.76 and root mean square error (RMSE) less than 1.42 cm^{-3} . Interestingly, there is a “shoulder” in the vertical distribution observed by CALIOP but not for the model prediction, which might due to the single Gaussian distribution adopted by NN model. Overall, the consistencies are better for the height less than $h_{m,i}$, but the predicted results have underestimation for the height larger than $h_{m,i}$ which might be caused by the deviation in MFASD. In addition, by taking the average MFNC as the parameter $N_{m,i}^*$ in Equation (2), the quasi real-time vertical profile of absorbing aerosols can be predicted finally.

Besides the monthly products validations, we also validated the predicted daily vertical distributions of dust and smoke aerosols by comparing with the altitude of biomass burning emissions injection and dust aerosol derived from CAMS and IASI. Figure 15 showed the comparison results for the predicted smoke and dust MFA on January 1, April 1, June 1 and October 1 in 2019. The correlation coefficients were from 0.48 to 0.63 with RMSE from 0.61 to 0.78 km. Comparing with the validation results of the monthly predictions, the performance of daily predictions slightly decreased, but the model can still provide rationale predictions. With regard to daily smoke MFA, the correlation coefficients were from 0.55 to 0.66 with RMSE from 0.36 to 0.48 km (Figure 16), which was slightly more accurate than it of the dust aerosol prediction. Overall, the established NN models can predict quasi real-time globally vertical distributions of dust and smoke aerosols, which is helpful for improving atmospheric correction of satellite remote sensing.

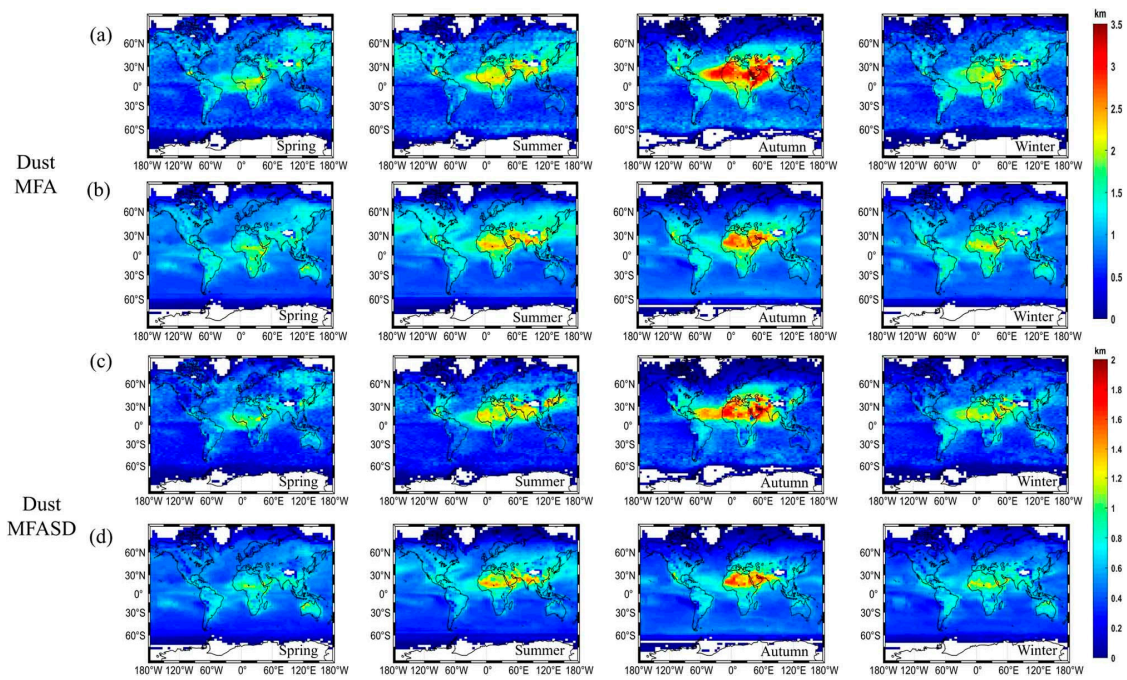


Figure 10. Comparisons between model predictions and CALIPSO observations for the dust aerosol. (a) CALIPSO observed MFA; (b) model predicted MFA; (c) CALIPSO observed MFASD; (d) model predicted MFASD. White shading indicates insufficient available data.

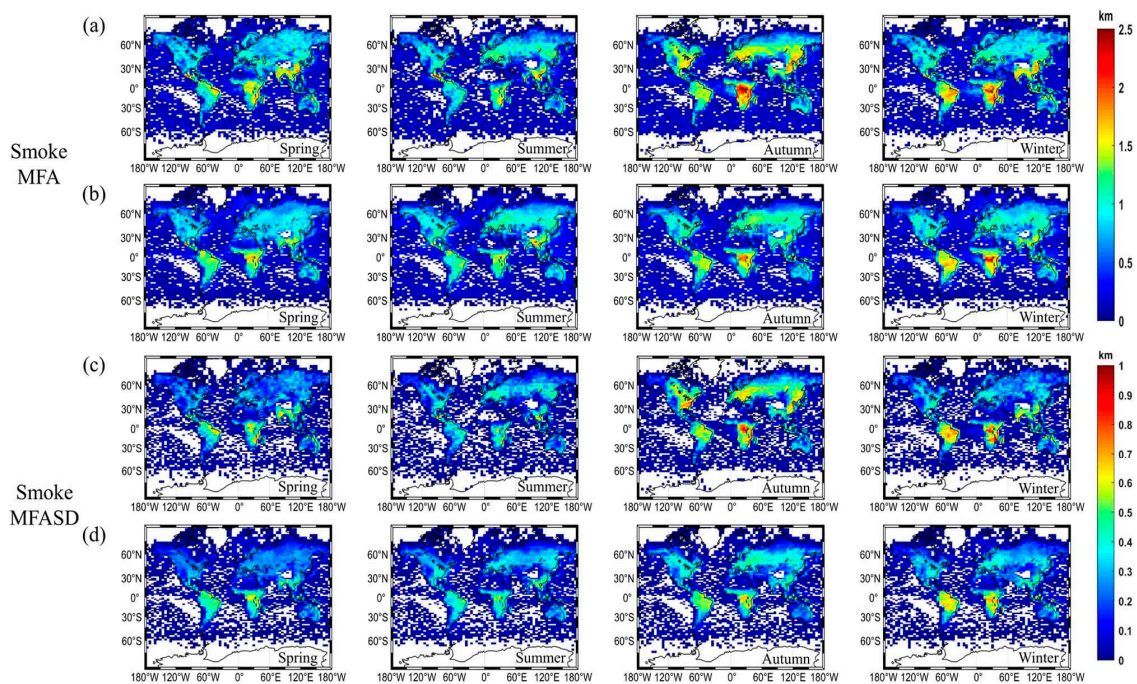


Figure 11. Comparisons between model predictions and CALIPSO observations for the smoke aerosol. (a) CALIPSO observed MFA; (b) model predicted MFA; (c) CALIPSO observed MFASD; (d) model predicted MFASD. White shading indicates insufficient available data.

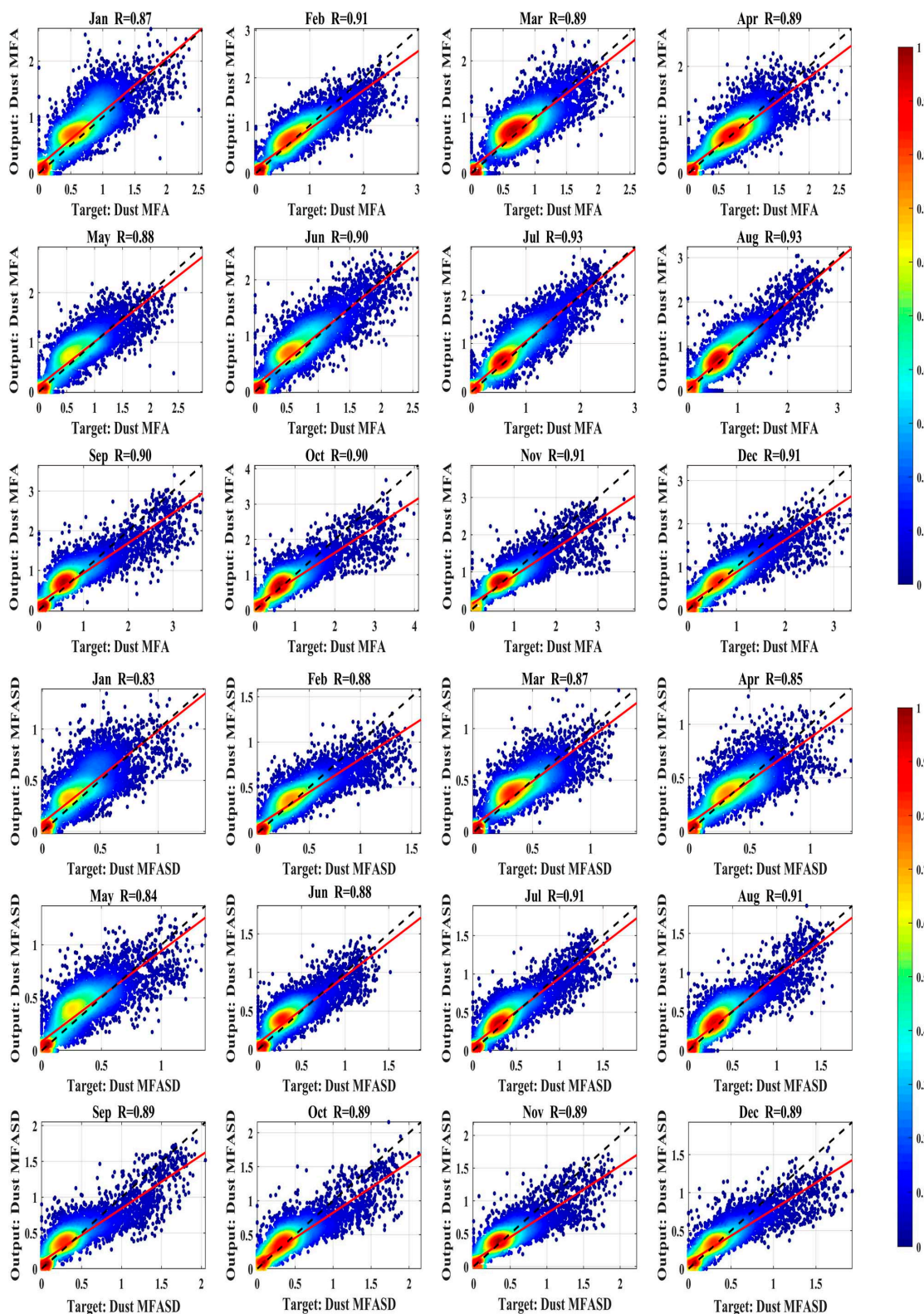


Figure 12. Correlation coefficients between model predicted and CALIPSO observed values of dust aerosol MFA (km) and MFASD (km) in different months.

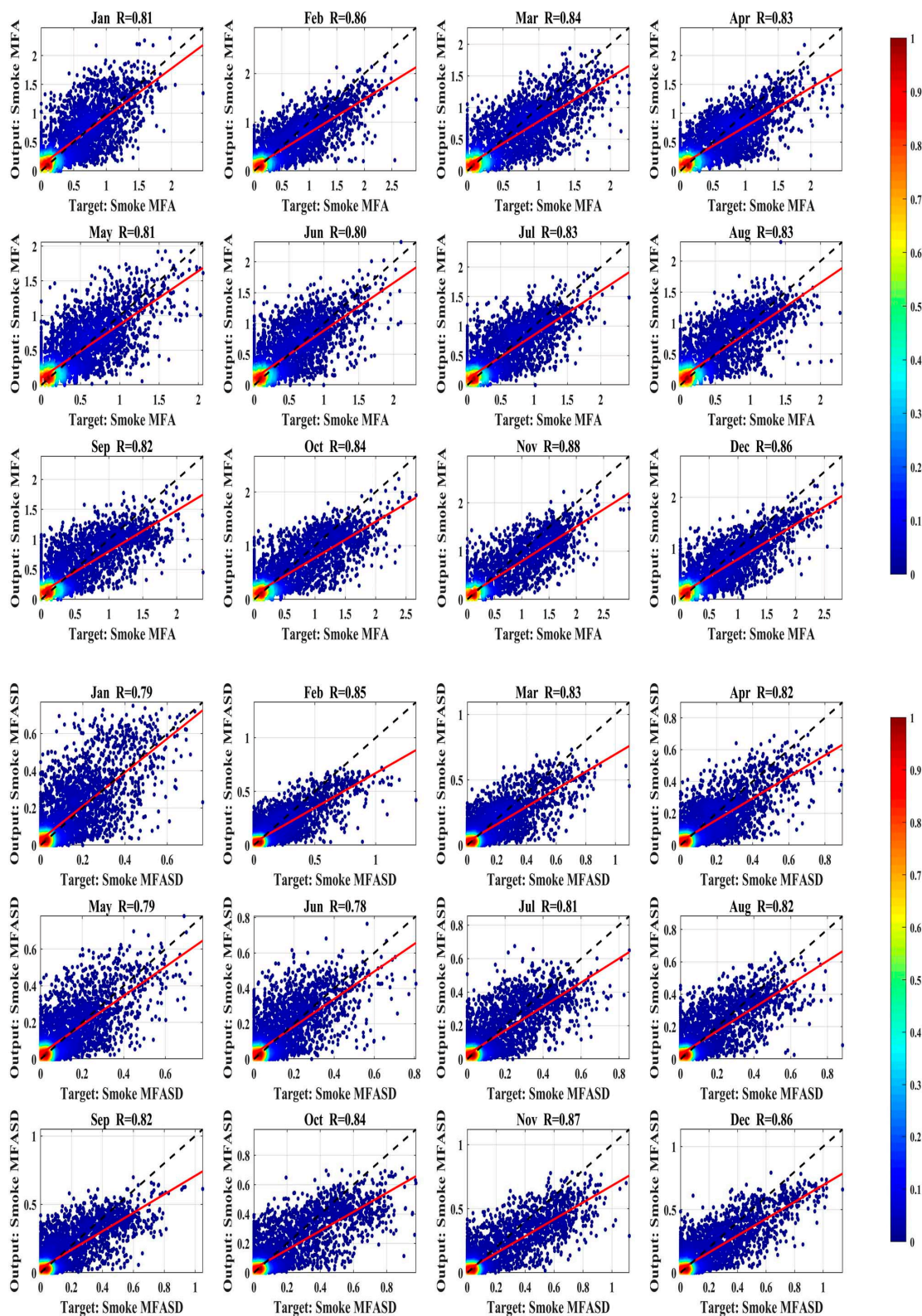


Figure 13. Correlation coefficients between model predicted and CALIPSO observed values of smoke aerosol MFA (km) and MFASD (km) in different months.

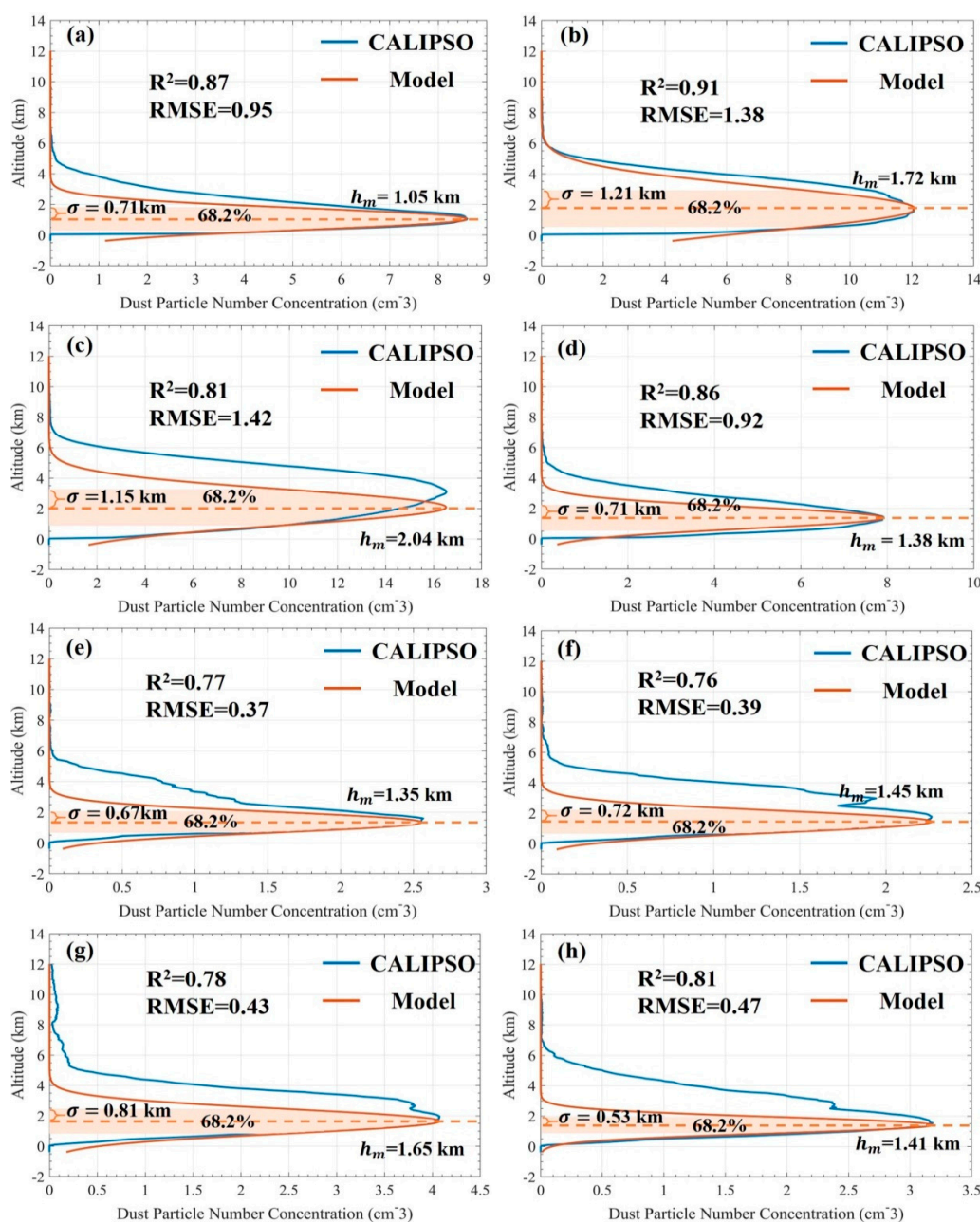


Figure 14. The comparisons of monthly mean vertical profile of dust and smoke particle number concentrations between model predictions and CALIPSO observations in 2016. (a) Dust aerosol in January; (b) dust aerosol in April; (c) dust aerosol in July; (d) dust aerosol in October; (e) smoke aerosol in January; (f) smoke aerosol in April; (g) smoke aerosol in July; (h) smoke aerosol in October.

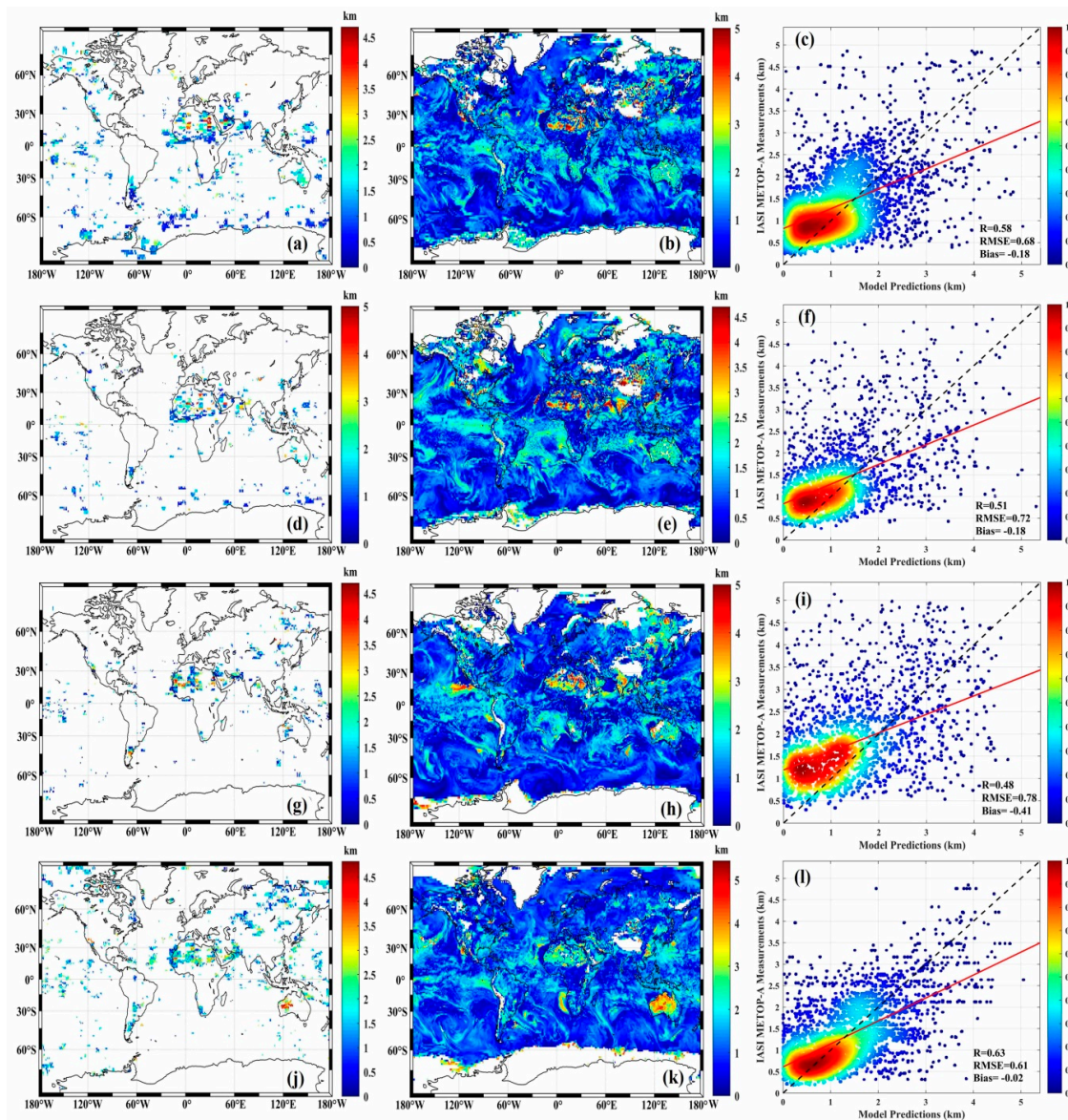


Figure 15. The validations on daily dust aerosol MFA predictions. (a), (d), (g) and (j) are the results for dust aerosol layer height observed by IASI on 1st January 2019, 1st April 2019, 1st June 2019, and 1st October 2019, respectively. (b), (e), (h), (k) are the model predicted dust aerosol MFA on 1st January 2019, 1st April 2019, 1st June 2019, and 1st October 2019, respectively. (c), (f), (i) and (l) are the scattering density plots comparisons of the dust aerosol MFA between model predicted and IASI observed values on 1st January 2019, 1st April 2019, 1st June 2019, and 1st October 2019, respectively.

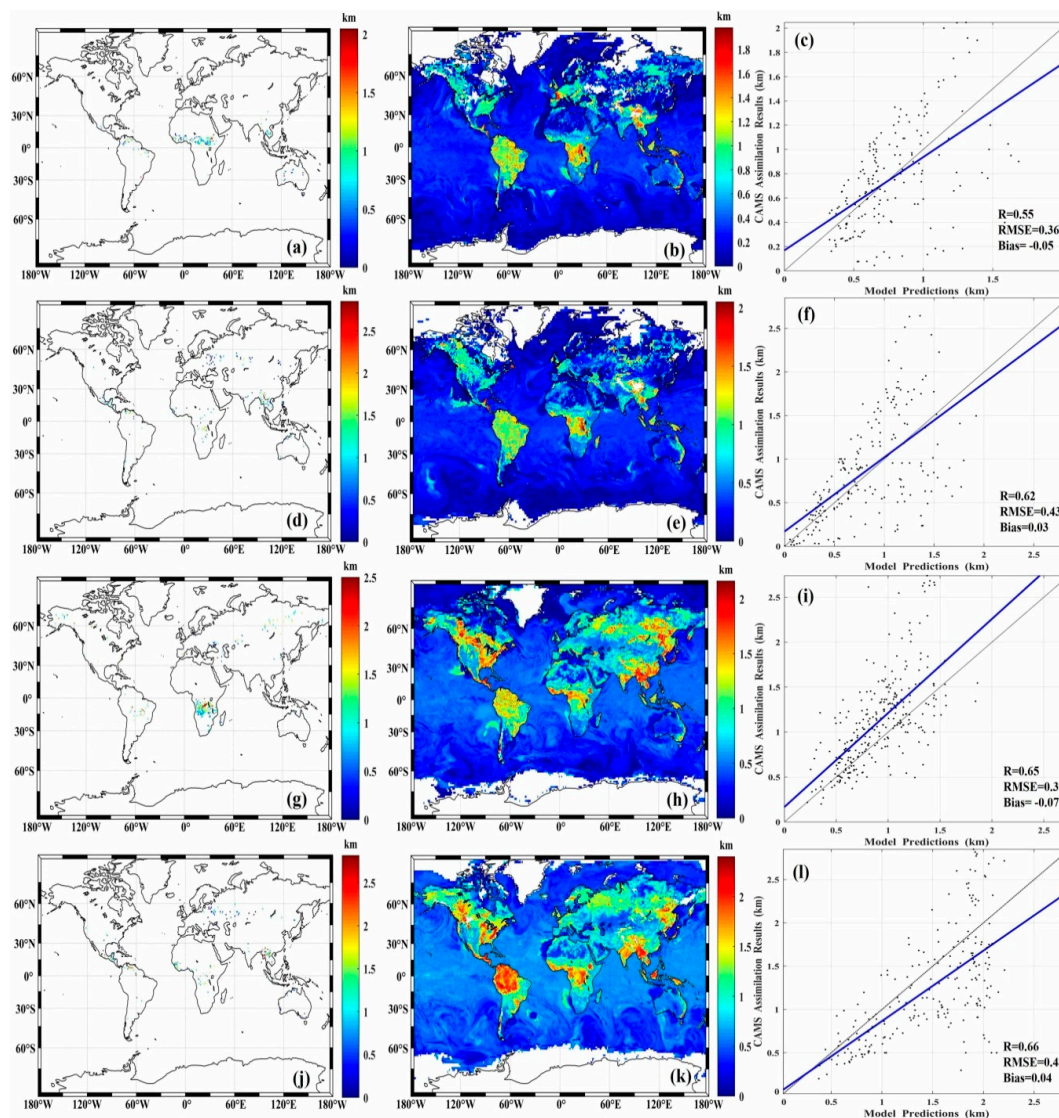


Figure 16. The validations on daily smoke aerosol MFA predictions. (a,d,g,j) are the mean altitude of biomass burning emissions injection derived by GFAS on 1st January 2019, 1st April 2019, 1st June 2019, and 1st October 2019, respectively; (b,e,h,k) are the model predicted smoke aerosol MFA on 1st January 2019, 1st April 2019, 1st June 2019, and 1st October 2019, respectively; (c,f,i,l) are the are the scattering plots comparisons of the dust aerosol MFA between model predicted and GFAS-derived mean altitude of biomass burning emissions injection on 1st January 2019, 1st April 2019, 1st June 2019, and 1st October 2019, respectively.

4. Discussion

4.1. Spatial-temporal Variations of Absorbing Aerosols

Our absorbing aerosol vertical distribution results are consistent with the findings of Huang et al. (2013) that aerosols were frequently observed at height from 0.5 to 2.5 km in western Australia and high occurrence frequency of smoke aerosols in biomass burning areas at 1 to 3 km height [27]. Alonso et al. (2019) also found smoke aerosols located at maximum altitudes below 2.5 km over the Amazon [29], which was consistent with our results that 68.2% of smoke aerosols were distributed at 0.4 to 2.6 km (inferred from MFA from 0.8 to 1.6 km, and MFASD from 0.4 to 1 km) in the Amazonian plain. Emmanouil et al. (2018) investigated climatological dust extinction coefficient profiles, and found that the maximum values of dust profile top height and dust center of mass were ~3 km and 2 km,

respectively, in winter in the central and eastern China [42], which was consistent with our results that dust was mainly distributed between 1.2 to 3.1 km. In addition, the significant long-range transmission features of dust aerosols from the Taklimakan and Gobi deserts into eastern China and western Pacific during boreal spring, as illustrated in Figures 2a and 3a, was consistent with the results from Emmanouil et al. (2018) that the altitude of transport of the dust layers was decreased from the Taklimakan Desert towards the Pacific during spring [42]. Air temperature variability may have an impact on the seasonal variations of the altitude of absorbing aerosols. Sheehan et al. (2001) explored the temperature dependence of secondary organic aerosol concentrations and found that air temperature likely had a negative influence on secondary organic aerosol partitioning and concentrations [43].

Recent research by Kang et al. (2017) (using OMI and EDGAR datasets) found that absorbing aerosols increased over East Asia from 2005 to 2016 [13]. Compared to their study, we divided the whole globe into land and ocean and found that absorbing aerosol trends show distinct differences over ocean and land. Furthermore, we revealed changing trends of vertical distribution characteristics. As mentioned in the results, the variation tendencies of absorbing aerosols were lower in the ocean than land due to the predominating land sources and transportation to the ocean. Indeed, Huang et al. (2015) reported that smoke originating from land is transported by wind to offshore waters [19]. Based on the SeaWiFS and MODIS products, Hsu et al. (2012) also derived similar variation trends in dust MFNC values, which were negative ($-3\% \text{ yr}^{-1}$ to $-8\% \text{ yr}^{-1}$) over the western United States but positive ($1\% \text{ yr}^{-1}$ to $6\% \text{ yr}^{-1}$) over North China [28]. Compared to their study, we investigated the vertical variation characteristics through satellite-measured absorbing aerosols products.

The vertical distribution of absorbing aerosols can have a considerable impact on the reflectance of the ocean-atmosphere coupling system due to the combination of atmospheric scattering and aerosol absorption, especially in visible light [2,3]. Shi et al. (2019) investigated smoke characteristics for different vegetation surfaces and found stronger negative radiative forcing efficiency in forest and peat regions [44]. In this study, we presented the spatial distribution of MFA, as shown in Figures 3 and 5, which should be helpful for further study on the impact of absorbing aerosols on solar radiation transfer in the Earth's systems. Huang et al. (2015) [19] investigated the most probable height (MPH) of dust and smoke aerosols and identified the occurrence frequency of the vertical profile characteristics of aerosols. The vertical distribution characteristics for both dust and smoke shown in Figures 4 and 7 suggest that absorbing aerosols varied seasonally in their vertical profiles, which may be influenced by aerosol sources, air temperature, and air pressure [11]. Specifically, the vertical profile of absorbing aerosols can be reflected by MFA and MFASD. Combining MFA and MFASD, we found that most smoke aerosols were distributed from the ground up to 2–4 km. Likewise, Alonso et al. (2019) found significant variability in smoke height, with altitudes ranging from near-surface up to 5 km, depending on biomass combustion emissions and their dissipation [29].

Compared to previous studies, we not only presented the vertical distribution characteristics of absorbing aerosols, but also revealed the long-term changes in dust and smoke aerosols over the ocean and land. It is worth noting that the differences in the rates of changes between land and ocean may be responsible for their different impacts on radiation forcing and meteorological conditions. As seen in Figure 5, most smoke aerosols were distributed in tropical rainforest and grassland regions, suggesting that the transportation of smoke aerosols is influenced by the monsoon climate. Khan et al. (2011) found that aerosol concentrations can be reduced in the atmosphere by monsoonal rainfall, especially near Pakistan [45], which can also be inferred from Figure 2. An overall increasing trend in MFNC of absorbing aerosols could have great impact not only on radiative forcing, but also on ocean ecosystems. For example, major external sources of phosphorus to the ocean are provided by the deposition of atmospheric aerosols, which are available for uptake by phytoplankton and exacerbate ocean acidification [46]. As shown in Figure 8c, dust MFNC increased at a ratio of $0.56 \text{ cm}^{-3} \text{ yr}^{-1}$, which could have an impact on oceanic primary productivity [5,47].

4.2. Predictions of Vertical Distributions of Absorbing Aerosols

In order to predict quasi real-time information of absorbing aerosols vertical distribution, NN models were trained and validated by monthly MFA and MFASD, which enable the prediction of the daily MFA and MFASD based on the atmospheric environment parameters. From Figures 10 and 12, it can be seen that global MFA and MFASD values of dust in the range of 0 to 1.2 km and 0 to 0.6 km, respectively, take up larger proportion because dust aerosol mainly locates in most of deserts and their surrounding regions. Although predicted results by model have slight anomalies during autumn, this model can rather accurately predict the MFA and MFASD of dust aerosol in most regions. The slight underestimation for the prediction results might be owing to the limitation of the quality of training dataset. There are more detailed variations in spatial distributions when we employed our model to the daily predictions. Kylling et al. (2018) found that there was a positive deviation of 0.5–0.8 km between IASI dust aerosol layer height and CALIOP extinction-weighted height, which explains our predictions bias [48]. Additionally, the discrepancy in definition between MFA and dust aerosol layer height might be another reason for prediction bias.

As for the prediction of the smoke aerosol, the results demonstrate that the NN model can effectively predict the vertical distribution parameters of smoke aerosols in the regions with low and middle concentrations values but has relative lower performance in high concentrations areas. For example, the prediction results over the ocean and some regions with low values are better than other places, which might be affected by lacking the accurate emissions data of daily combustion of biomass and fossil fuels. Vadrevu et al. (2015) and Yao et al. (2018) found smoke plumes extended less than 5 km [21,49], which are consistent with our results. Compared to dust predictions, smoke predictions have better stability which might due to their different inputs and small number of validation samples. On the other hand, the mean altitude of biomass burning emissions injection is more consistent with the MFA values than dust aerosol layer height in actual meaning. With regard to considerations of input data, more accurate input products might decrease the prediction bias.

The vertical profile characteristics of absorbing aerosols can have a substantial influence on the accuracy of atmospheric correction. The globally seasonal vertical distributions of absorbing aerosols derived by this study can provide an important prior knowledge. Previous research has mainly focused on the regional scale or specific aerosol types, which is insufficient for addressing globally atmospheric correction [50]. In addition, although satellite observations such as the CALIPSO can provide global monthly vertical distribution products of absorbing aerosols, it is still difficult to meet the requirement for the atmospheric correction application which needs real-time information on the absorbing aerosol profile. The prediction models established by this study can provide real-time absorbing aerosol profile as the inputs of these models are based on the operationally reanalyze ECMWF data. Thus, these prediction models could be helpful for global aerosol related researches and atmospheric correction of satellite remote sensing.

5. Conclusions

In this study, we have investigated the spatiotemporal variations of the vertical distributions for global absorbing aerosols based on CALIPSO data from 2006 to 2016. We also analyzed the long-term changing tendencies of MFA and MFNC over land and ocean. In addition, we proposed prediction models for the vertical distribution information of absorbing aerosols based on the ECMWF reanalysis meteorological and radiative data.

Our results showed that the high MFNC values mainly occurred near source regions, e.g., Sahara Desert, Arabian Desert, and other deserts for dust aerosol, and tropical rainforest and grassland regions for smoke aerosol, and their spatial distributions varied with seasons. Generally, the spatiotemporal distributions of MFA and MFASD exhibited regional properties and varied under different geographical circumstances and meteorological conditions (e.g., temperature, relative humidity, pressure, and wind velocity). We found that dust aerosols were more efficiently transported to the adjacent ocean and other non-desert regions such as the Central Atlantic, North China

Plain, and Arabian Sea. In addition, dust MFNC increased faster ($0.98 \text{ cm}^{-3} \text{ yr}^{-1}$) over land than over the ocean ($0.56 \text{ cm}^{-3} \text{ yr}^{-1}$) from 2007 to 2016. High increasing dust MFNC rates (8% to 15% yr^{-1}) were found in the polar regions. With regard to the changing trends in vertical distribution of absorbing aerosols, the global mean MFA of dust and smoke decreased by -2.7 m yr^{-1} and -1.7 m yr^{-1} , respectively. Dust MFA decreased more strongly over the ocean (-4.9 m yr^{-1}), indicating possible enhanced deposition of dust aerosol particles over the ocean and the aerosol contamination from aerosol transportation and sedimentation should be paid more emphasis in non-aerosol source regions.

Validation results showed that the model predicted vertical distributions were consistent with the CALIPSO observed data, indicating that the NN models can basically reproduce the observed information. Although these NN models have the capability to predict the vertical distributions of absorbing aerosols from the atmospheric environment parameters, they are still unable to clearly explain the internal physical mechanisms. Therefore, the prediction model based on the physical mechanisms still needs to be developed in future. Overall, this method can roughly estimate the vertical distributions of absorbing aerosols when no real-time vertical observation information is available on a global scale, which should be helpful for estimating radiative forcing and atmospheric correction of satellite remote sensing.

The vertical distributions of absorbing aerosols have received widespread attention due to their significant radiative forcing effects and environmental impacts. Our results demonstrated increasing MFNC and decreasing MFA of absorbing aerosols over land and ocean, indicating an urgency to protect the atmospheric environment. Moreover, the increase in MFNC and decrease in MFA indicates possible enhanced deposition over the ocean, which might input more nutrients into the ocean and influence marine ecosystems. The effects of changing vertical distributions of absorbing aerosols on radiative forcing and marine ecosystems, and the application of the prediction models to atmospheric correction of satellite ocean color remote sensing needs further investigations in the future.

Author Contributions: Conceptualization, Z.S., X.H., Y.B.; methodology, Z.S., X.H., Y.B.; data analyses and field investigation, Z.S., X.H., Y.B., D.W.; visualization, D.W., Z.H.; data interpretation, Z.S., D.W., Z.H., F.G., Q.Z.; writing—original draft, Z.S., X.H., Y.B.; writing—review and editing, X.H., Y.B., D.W., Z.H., supervision, X.H., Y.B., F.G., Q.Z.; project administration, X.H. and Y.B. All authors have read and agreed to the published version of the manuscript.

Funding: This research was funded by the National Key Research and Development Program of China (Grant #2017YFA0603003), the National Natural Science Foundation of China (Grants #41825014, #41676172, #41676170, #41706207 and #41621064), the Global Change and Air-Sea Interaction Project of China (Grants #GASI-02-SCS-YGST2-01, #GASI-02-PAC-YGST2-01 and #GASI-02-IND-YGST2-01), the Key Special Project for Introduced Talents Team of Southern Marine Science and Engineering Guangdong Laboratory (Guangzhou) (GML2019ZD0602).

Acknowledgments: We are highly grateful to acknowledge the considerable services of NASA Langley Research Center Atmospheric Science Data Center for providing CALIPSO data utilized in this study. We are highly grateful to acknowledge the ECMWF (<https://apps.ecmwf.int/datasets/>) for providing the ERA5, CAMS, and IASI dataset in this study. CALIPSO data can be obtained from the NASA Langley Research Center Atmospheric Science Data Center (<http://eosweb.larc.nasa.gov/>). We thank the satellite ground station, satellite data processing & sharing center, and marine satellite data online analysis platform (SatCO2) of SOED/SIO/MNR for their help on data collection and processing.

Conflicts of Interest: The authors declare no conflict of interest.

References

1. Gordon, H.R.; Du, T.; Zhang, T. Remote sensing of ocean color and aerosol properties: Resolving the issue of aerosol absorption. *Appl. Opt.* **1997**, *36*, 8670–8684. [[CrossRef](#)] [[PubMed](#)]
2. Myhre, G.; Bellouin, N.; Berglen, T.F.; Berntsen, T.K.; Boucher, O.; Grini, A.; Ivar, S.A.M.; Johnsrud, I.; Micheal, I.M.; Stordal, F.; et al. Comparison of the radiative properties and direct radiative effect of aerosols from a global aerosol model and remote sensing data over ocean. *Tellus B Chem. Phys. Meteorol.* **2007**, *59*, 115–129. [[CrossRef](#)]
3. Duforêt, L.; Frouin, R.; Dubuisson, P. Importance and estimation of aerosol vertical structure in satellite ocean-color remote sensing. *Appl. Opt.* **2007**, *46*, 1107–1119. [[CrossRef](#)] [[PubMed](#)]

4. Taubman, B.F.; Marufu, L.T.; Vant-Hull, B.L.; Piety, C.A.; Doddridge, B.G.; Dickerson, R.R.; Li, Z. Smoke over haze: Aircraft observations of chemical and optical properties and the effects on heating rates and stability. *J. Geophys. Res. Space Phys.* **2004**, *109*, D02206-n/a. [[CrossRef](#)]
5. Mahowald, N.M. Aerosol Indirect Effect on Biogeochemical Cycles and Climate. *Science* **2011**, *334*, 794–796. [[CrossRef](#)]
6. Wang, M.; Jiang, L. Atmospheric Correction Using the Information From the Short Blue Band. *IEEE Trans. Geosci. Remote Sens.* **2018**, *56*, 6224–6237. [[CrossRef](#)]
7. Gordon, H.R. Atmospheric correction of ocean color imagery in the Earth Observing System era. *J. Geophys. Res. Space Phys.* **1997**, *102*, 17081–17106. [[CrossRef](#)]
8. Zhang, M.; Hu, C.; Barnes, B.B. Performance of POLYMER Atmospheric Correction of Ocean Color Imagery in the Presence of Absorbing Aerosols. *IEEE Trans. Geosci. Remote Sens.* **2019**, *57*, 6666–6674. [[CrossRef](#)]
9. Bond, T.C.; Doherty, S.J.; Fahey, D.W.; Forster, P.M.D.F.; Berntsen, T.; DeAngelo, B.J.; Flanner, M.G.; Ghan, S.; Kärcher, B.; Koch, D.; et al. Bounding the role of black carbon in the climate system: A scientific assessment. *J. Geophys. Res. Atmos.* **2013**, *118*, 5380–5552. [[CrossRef](#)]
10. Charlson, R.J.; Schwartz, S.E.; Hales, J.M.; Cess, R.D.; Coakley, J.A.; Hansen, J.E.; Hofmann, D.J.; Schwarz-Sommer, Z.; Saedler, H.; Sommer, H.; et al. Climate Forcing by Anthropogenic Aerosols. *Science* **1992**, *255*, 423–430. [[CrossRef](#)]
11. Lin, L.; Gettelman, A.; Fu, Q.; Xu, Y. Simulated differences in 21st century aridity due to different scenarios of greenhouse gases and aerosols. *Clim. Chang.* **2018**, *146*, 407–422. [[CrossRef](#)]
12. Gao, B.-C.; Montes, M.J.; Davis, C.O.; Goetz, A.F. Atmospheric correction algorithms for hyperspectral remote sensing data of land and ocean. *Remote Sens. Environ.* **2009**, *113*, S17–S24. [[CrossRef](#)]
13. Kang, L.; Chen, S.; Huang, J.; Zhao, S.; Ma, X.; Yuan, T.; Zhang, X.; Xie, T. The Spatial and Temporal Distributions of Absorbing Aerosols over East Asia. *Remote Sens.* **2017**, *9*, 1050. [[CrossRef](#)]
14. Han, Y.; Wu, Y.-H.; Wang, T.; Zhuang, B.; Li, S.; Zhao, K. Impacts of elevated-aerosol-layer and aerosol type on the correlation of AOD and particulate matter with ground-based and satellite measurements in Nanjing, southeast China. *Sci. Total Environ.* **2015**, *532*, 195–207. [[CrossRef](#)]
15. Guo, J.P.; Zhang, X.Y.; Wu, Y.R.; Zhaxi, Y.; Che, H.Z.; La, B.; Wang, W.; Li, X.W. Spatio-temporal variation trends of satellite-based aerosol optical depth in China during 1980–2008. *Atmos. Environ.* **2011**, *45*, 6802–6811. [[CrossRef](#)]
16. Ma, X.; Bartlett, K.; Harmon, K.; Yu, F. Comparison of AOD between CALIPSO and MODIS: Significant differences over major dust and biomass burning regions. *Atmos. Meas. Tech.* **2013**, *6*, 2391–2401. [[CrossRef](#)]
17. Young, S.A.; Vaughan, M.; Kuehn, R.E.; Winker, D.M. The Retrieval of Profiles of Particulate Extinction from Cloud–Aerosol Lidar and Infrared Pathfinder Satellite Observations (CALIPSO) Data: Uncertainty and Error Sensitivity Analyses. *J. Atmos. Ocean. Technol.* **2013**, *30*, 395–428. [[CrossRef](#)]
18. Cavalieri, O.; Cairo, F.; Fierli, F.; Di Donfrancesco, G.; Snels, M.; Viterbini, M.; Cardillo, F.; Chatenet, B.; Formenti, P.; Marticorena, B.; et al. Variability of aerosol vertical distribution in the Sahel. *Atmos. Chem. Phys. Discuss.* **2010**, *10*, 12005–12023. [[CrossRef](#)]
19. Huang, J.; Guo, J.; Wang, F.; Liu, Z.; Jeong, M.-J.; Yu, H.; Zhang, Z.-B. CALIPSO inferred most probable heights of global dust and smoke layers. *J. Geophys. Res. Atmos.* **2015**, *120*, 5085–5100. [[CrossRef](#)]
20. Jacobson, M.Z. Strong radiative heating due to the mixing state of black carbon in atmospheric aerosols. *Nature* **2001**, *409*, 695–697. [[CrossRef](#)]
21. Yao, J.; Raffuse, S.M.; Brauer, M.; Williamson, G.J.; Bowman, D.M.; Johnston, F.H.; Henderson, S.B. Predicting the minimum height of forest fire smoke within the atmosphere using machine learning and data from the CALIPSO satellite. *Remote Sens. Environ.* **2018**, *206*, 98–106. [[CrossRef](#)]
22. Mao, X.; Shen, T.; Feng, X. Prediction of hourly ground-level PM 2.5 concentrations 3 days in advance using neural networks with satellite data in eastern China. *Atmos. Pollut. Res.* **2017**, *8*, 1005–1015. [[CrossRef](#)]
23. Nabavi, S.O.; Haimberger, L.; Abbasi, R.; Samimi, C. Prediction of aerosol optical depth in West Asia using deterministic models and machine learning algorithms. *Aeolian Res.* **2018**, *35*, 69–84. [[CrossRef](#)]
24. Kow, P.-Y.; Wang, Y.-S.; Zhou, Y.; Kao, I.-F.; Issermann, M.; Chang, L.-C.; Chang, F.-J. Seamless integration of convolutional and back-propagation neural networks for regional multi-step-ahead PM2.5 forecasting. *J. Clean. Prod.* **2020**, *261*, 121285. [[CrossRef](#)]

25. Park, Y.; Kwon, B.; Heo, J.; Hu, X.; Liu, Y.; Moon, T. Estimating PM_{2.5} concentration of the conterminous United States via interpretable convolutional neural networks. *Environ. Pollut.* **2020**, *256*, 113395. [[CrossRef](#)] [[PubMed](#)]
26. Xiao, F.; Wong, M.S.; Lee, K.-H.; Campbell, J.R.; Shea, Y.-K. Retrieval of dust storm aerosols using an integrated Neural Network model. *Comput. Geosci.* **2015**, *85*, 104–114. [[CrossRef](#)]
27. Huang, L.; Jiang, J.H.; Tackett, J.L.; Su, H.; Fu, R. Seasonal and diurnal variations of aerosol extinction profile and type distribution from CALIPSO 5-year observations. *J. Geophys. Res. Atmos.* **2013**, *118*, 4572–4596. [[CrossRef](#)]
28. Hsu, N.C.; Gautam, R.; Sayer, A.M.; Bettenhausen, C.; Li, C.; Jeong, M.J.; Tsay, S.-C.; Holben, B.N. Global and regional trends of aerosol optical depth over land and ocean using SeaWiFS measurements from 1997 to 2010. *Atmos. Chem. Phys. Discuss.* **2012**, *12*, 8037–8053. [[CrossRef](#)]
29. Gonzalez-Alonso, L.; Martin, M.V.; Kahn, R.A. Biomass-burning smoke heights over the Amazon observed from space. *Atmos. Chem. Phys. Discuss.* **2019**, *19*, 1685–1702. [[CrossRef](#)]
30. Winker, D.M.; Vaughan, M.; Omar, A.; Hu, Y.; Powell, K.A.; Liu, Z.; Hunt, W.H.; Young, S.A. Overview of the CALIPSO Mission and CALIOP Data Processing Algorithms. *J. Atmos. Ocean. Technol.* **2009**, *26*, 2310–2323. [[CrossRef](#)]
31. Pan, H.; Wang, M.; Kumar, K.R.; Lu, H.; Mamtimin, A.; Huo, W.; Yang, X.; Yang, F.; Zhou, C. Seasonal and vertical distributions of aerosol type extinction coefficients with an emphasis on the impact of dust aerosol on the microphysical properties of cirrus over the Taklimakan Desert in Northwest China. *Atmos. Environ.* **2019**, *203*, 216–227. [[CrossRef](#)]
32. Rémy, S.; Veira, A.; Paugam, R.; Sofiev, M.; Kaiser, J.W.; Marengo, F.; Burton, S.P.; Benedetti, A.; Engelen, R.; Ferrare, R.; et al. Two global data sets of daily fire emission injection heights since 2003. *Atmos. Chem. Phys. Discuss.* **2017**, *17*, 2921–2942. [[CrossRef](#)]
33. Klüser, L.; Banks, J.R.; Martynenko, D.; Bergemann, C.; Brindley, H.; Holzer-Popp, T. Information content of space-borne hyperspectral infrared observations with respect to mineral dust properties. *Remote Sens. Environ.* **2015**, *156*, 294–309. [[CrossRef](#)]
34. Barnes, J.E.; Sharma, N.C.P.; Kaplan, T.B. Atmospheric aerosol profiling with a bistatic imaging lidar system. *Appl. Opt.* **2007**, *46*, 2922–2929. [[CrossRef](#)] [[PubMed](#)]
35. Guo, J.; Xia, F.; Zhang, Y.; Liu, H.; Li, J.; Lou, M.; He, J.; Yan, Y.; Wang, F.; Min, M.; et al. Impact of diurnal variability and meteorological factors on the PM_{2.5}—AOD relationship: Implications for PM_{2.5} remote sensing. *Environ. Pollut.* **2017**, *221*, 94–104. [[CrossRef](#)]
36. Li, X.; Cheng, X.; Wu, W.; Wang, Q.; Tong, Z.; Zhang, X.; Deng, D.; Li, Y. Forecasting of bioaerosol concentration by a Back Propagation neural network model. *Sci. Total Environ.* **2020**, *698*, 134315. [[CrossRef](#)]
37. Lakshmi, N.B.; Babu, S.S.; Nair, V.S. Recent Regime Shifts in Mineral Dust Trends Over South Asia From Long-Term CALIPSO Observations. *IEEE Trans. Geosci. Remote Sens.* **2019**, *57*, 1–5. [[CrossRef](#)]
38. Kazil, J.; Stier, P.; Zhang, K.; Quaas, J.; Kinne, S.; O'Donnell, D.; Rast, S.; Esch, M.; Ferrachat, S.; Lohmann, U.; et al. Aerosol nucleation and its role for clouds and Earth's radiative forcing in the aerosol-climate model ECHAM5-HAM. *Atmos. Chem. Phys. Discuss.* **2010**, *10*, 10733–10752. [[CrossRef](#)]
39. Peers, F.; Waquet, F.; Cornet, C.; Dubuisson, P.; Ducos, F.; Goloub, P.; Szczap, F.; Tanre, D.; Thieuleux, F. Absorption of aerosols above clouds from POLDER/PARASOL measurements and estimation of their direct radiative effect. *Atmos. Chem. Phys. Discuss.* **2015**, *15*, 4179–4196. [[CrossRef](#)]
40. Huang, G.-B. Learning capability and storage capacity of two-hidden-layer feedforward networks. *IEEE Trans. Neural Netw.* **2003**, *14*, 274–281. [[CrossRef](#)]
41. Dahutia, P.; Pathak, B.; Bhuyan, P.K. Vertical distribution of aerosols and clouds over north-eastern South Asia: Aerosol-cloud interactions. *Atmos. Environ.* **2019**, *215*, 116882. [[CrossRef](#)]
42. Proestakis, E.; Amiridis, V.; Marinou, E.; Georgoulas, A.K.; Solomos, S.; Kazadzis, S.; Chimot, J.; Che, H.; Alexandri, G.; Biniotoglou, I.; et al. Nine-year spatial and temporal evolution of desert dust aerosols over South and East Asia as revealed by CALIOP. *Atmos. Chem. Phys. Discuss.* **2018**, *18*, 1337–1362. [[CrossRef](#)]
43. Sheehan, P.E.; Bowman, F.M. Estimated effects of temperature on secondary organic aerosol concentrations. *Environ. Sci. Technol.* **2001**, *35*, 2129–2135. [[CrossRef](#)]
44. Shi, S.; Cheng, T.; Gu, X.; Guo, H.; Wu, Y.; Wang, Y. Biomass burning aerosol characteristics for different vegetation types in different aging periods. *Environ. Int.* **2019**, *126*, 504–511. [[CrossRef](#)] [[PubMed](#)]

45. Alam, K.; Qureshi, S.; Blaschke, T. Monitoring spatio-temporal aerosol patterns over Pakistan based on MODIS, TOMS and MISR satellite data and a HYSPLIT model. *Atmos. Environ.* **2011**, *45*, 4641–4651. [[CrossRef](#)]
46. Nenes, A.; Krom, M.D.; Mihalopoulos, N.; Van Cappellen, P.; Shi, Z.; Bougiatioti, A.; Zampas, P.; Herut, B. Atmospheric acidification of mineral aerosols: A source of bioavailable phosphorus for the oceans. *Atmos. Chem. Phys. Discuss.* **2011**, *11*, 6265–6272. [[CrossRef](#)]
47. Jickells, T.; An, Z.S.; Andersen, K.K.; Baker, A.R.; Bergametti, G.; Brooks, N.; Cao, J.; Boyd, P.W.; Duce, R.A.; Hunter, K.A.; et al. Global Iron Connections Between Desert Dust, Ocean Biogeochemistry, and Climate. *Science* **2005**, *308*, 67–71. [[CrossRef](#)]
48. Kylling, A.; Vandenbussche, S.; Capelle, V.; Cuesta, J.; Klüser, L.; Lelli, L.; Holzer-Popp, T.; Stebel, K.; Veefkind, P. Comparison of dust-layer heights from active and passive satellite sensors. *Atmos. Meas. Tech.* **2018**, *11*, 2911–2936. [[CrossRef](#)]
49. Vadrevu, K.P.; Lasko, K.; Giglio, L.; Justice, C. Vegetation fires, absorbing aerosols and smoke plume characteristics in diverse biomass burning regions of Asia. *Environ. Res. Lett.* **2015**, *10*, 105003. [[CrossRef](#)]
50. Myhre, G.; Samset, B.; Schulz, M.; Balkanski, Y.; Bauer, S.; Berntsen, T.K.; Bian, H.; Bellouin, N.; Chin, M.; Diehl, T.; et al. Radiative forcing of the direct aerosol effect from AeroCom Phase II simulations. *Atmos. Chem. Phys. Discuss.* **2013**, *13*, 1853–1877. [[CrossRef](#)]



© 2020 by the authors. Licensee MDPI, Basel, Switzerland. This article is an open access article distributed under the terms and conditions of the Creative Commons Attribution (CC BY) license (<http://creativecommons.org/licenses/by/4.0/>).